Effect of compact and elongated configurations on the spontaneous and induced fission of Fm isotopes

Amandeep Kaur,* Nitin Sharma, and Manoj K. Sharma
School of Physics and Materials Science, Thapar Institute of Engineering and Technology, Patiala 147004, India

(Received 27 January 2021; accepted 10 March 2021; published 25 March 2021)

The spontaneous fission (SF) analysis of even mass $^{242-260}$Fm isotopes is carried out using a preformed cluster model based on quantum mechanical fragmentation theory. The deformation effects are included up to the quadrupole (β_2) deformed nuclei with optimum orientations ($\theta_i^{\text{opt.}}$) leading to hot-compact (side-to-side) and cold-elongated (tip-to-tip) configurations. The spherical and hot-compact deformed configurations of decay fragments result in the symmetric fragment mass distributions for Fm isotopes; however, the symmetric peak gets sharper with an increase in the neutron (N) number of the parent nucleus. In the case of cold orientations, a transition from two-peaked (asymmetric fission) to three-peaked (multimodal fission) mass distribution is observed with an increase in the mass number of Fm. The SF half-lives ($T_{1/2}^{\text{SF}}$) are calculated using the neck-length parameter (ΔR) for $^{242-260}$Fm isotopes and compared with the experimental data. Besides this, the induced fission of Fm isotopes is studied within the dynamical cluster-decay model. The energy dependence of fission fragment mass distributions and the isotopic dependence is analyzed at energy range $E^* = 5$–42 MeV. In addition, the role of temperature-dependent deformations in the fission dynamics is also explored.

DOI: 10.1103/PhysRevC.103.034618

I. INTRODUCTION

The nuclear fission process, the splitting of the atomic nucleus into two or more fragments, has a significant role in the generation of electric power, the stability of superheavy nuclei, the termination of the r-nucleosynthesis process, and the generation of exotic nuclear isotopes. In addition, the fission decay products have many industrial and medical applications. It is therefore important to have an appropriate knowledge of the fission fragment mass distributions of heavy nuclei. Several experimental and theoretical efforts have been made to analyze the properties of nascent fission fragments, and it has been observed that macroscopic-microscopic effects play an important role in fission dynamics [1–5].

The literature shows some exceptional observations [3–9] in reference to fission fragment mass distributions. For example, the ^{180}Hg nucleus disintegrates into asymmetric fragmentation; however, it is supposed to decay via symmetric fission fragments, i.e., ^{90}Zr + ^{90}Zr having the magic neutron number $N = 50$ [3,4]. The n-induced fission of the ^{238}U nucleus at higher energies ($E_n = 50$–60 MeV) has maintained the two-humped mass asymmetric distribution, where shell effects are expected to vanish at such higher energies [5]. Moreover, the actinides are known to have an asymmetric fission pattern, but the first observation of a transition from asymmetric to symmetric fission has been measured in the region of mass $A = 256$–258 of Fm isotopes [7,8]. Such competing emergence among the symmetric and the asymmetric fission is mainly associated with deformed magic shell effects [2]. Apart from this, the tip-to-tip (equatorial *or* elongated) and side-to-side (polar *or* compact) configurations of nuclei have great impact on the formation and decay dynamics of a nucleus [10,11]. In view of the above, we require a thorough analysis of fission fragment mass distributions in reference to the macroscopic-microscopic effects, deformations, orientations, angular momentum, and energy dependence of fission observables for a wide isotopic range.

In the present manuscript, the spontaneous fission (SF) and the induced fission (IF) of fermium (Fm) isotopes having even mass number $A = 242$–260 are studied. It would be interesting to study the fission mechanism of Fm isotopes as they may exhibit a symmetric profile due to presence of two-proton magic Sn ($Z = 50$) mass-symmetric nuclei. Earlier, one of us and collaborators have studied the decay of the ^{254}Fm* compound nucleus (CN) formed in the ^{11}B + ^{243}Am reaction in a wide excitation energy range [12]. The obtained results suggest that deformation and orientation effects play important roles in the fission dynamics [12]. To analyze the IF dynamics, we have extended this study to other isotopes, i.e., $^{242-260}$Fm* formed in ^{11}B + $^{231-249}$Am reactions at excitation energies $E^* = 5$–42 MeV. The analysis of spontaneous fission and induced fission is worked out using the preformed cluster model (PCM) [13–16] and the dynamical cluster-decay model (DCM) [17–21], respectively.

The aim of this work is (i) to analyze the spontaneous as well as the induced fission of Fm isotopes having mass number $A = 242$–260; (ii) to examine the role of deformations and orientations of decay fragments in the structure of the fragmentation potential V(η, R) and the preformation probability (P_0); (iii) to investigate the impact of the excitation energy (E^*), the angular momentum (ℓ), and the neutron (N) number

*amanganday@gmail.com

 ©2021 American Physical Society

of fissioning nuclei on fission fragment mass distributions; (iv) to study the possibility of multimodal fission, i.e., the existence of both symmetric and asymmetric fission in Fm isotopes; and (v) to identify the nascent light (A_L) and heavy (A_H) fission fragments to analyze the role of spherical and deformed magic shell closure.

This manuscript is organized as follows: The description of cluster decay models based on quantum mechanical fragmentation theory is given in Sec. II. The calculations of spontaneous fission and induced fission of Fm isotopes and their corresponding discussions are presented in Sec. III, and finally the conclusions drawn are summarized in Sec. IV.

II. METHODOLOGY

In the present work, the SF and IF of fermium isotopes is studied within the framework of the PCM [13–16] and the DCM [17–21], respectively. These methods are based on the quantum mechanical fragmentation theory [22–24] which is governed via the collective coordinates of mass (and charge) asymmetry $\eta = (A_1 - A_2)/(A_1 + A_2)$, relative separation distance (R), multipole deformations ($\beta_{\lambda i}$), and orientations (θ_i), where $i = 1$ and 2 correspond to heavy (A_1 or A_H) and light (A_2 or A_L) nuclei in the same plane. The main ingredient of this methodology is the collective fragmentation potential $V_R(\eta, T)$ that brings the structural effects of the parent nucleus into the formalism and is calculated at fixed $R = R_a$ (the entry point of the penetration path) as

$$V_R(\eta, T) = \sum_{i=1}^{2}[V_{\rm LDM}(A_i, Z_i, T)] + \sum_{i=1}^{2}[\delta U_i]\exp\left(-T^2/T_0^2\right) + V_C(R, Z_i, \beta_{\lambda i}, \theta_i, T) + V_P(R, A_i, \beta_{\lambda i}, \theta_i, T) + V_\ell(R, A_i, \beta_{\lambda i}, \theta_i, T). \quad (1)$$

Here, $V_{\rm LDM}$, the T-dependent macroscopic liquid drop model, is taken from Davidson *et al.* [25], which is based on the semiempirical mass formula of Seeger [26]. δU, the "empirical" microscopic shell correction as stated in Ref. [27], is also made T dependent in reference to Ref. [28]. Both $V_{\rm LDM}$ and δU, the parts of the binding energy (B.E.), are obtained by using the macroscopic-microscopic renormalization method of Strutinsky [29]. The macroscopic ($V_{\rm LDM}$) and microscopic (δU) parts of the B.E. play an important role in deciding the symmetric and asymmetric division of the fissioning nucleus. Moreover, the δU term is strongly affected by the excitation energy of the nucleus [see Eq. (1)] and becomes silent at sufficiently higher energies [28]. In Eq. (1), V_C, V_P, and V_ℓ are the Coulomb, proximity, and centrifugal potentials, respectively (for further description, see Ref. [21]). The prox2000 version of the proximity potential [30,31] is considered for the calculations of induced fission and spontaneous fission.

The static (T-independent) deformations of fragments are taken up to quadrupole deformations (β_{2i}) from the theoretical estimates of Möller *et al.* [32], and the "optimum" orientations $\theta_i^{\rm opt.}$ for hot-compact and cold-elongated configurations are taken from Table 1 of Ref. [11]. The orientations of decay fragments are uniquely fixed on the basis of the (+ or −) sign of their corresponding β_{2i}, which manifest in the form of the hot-compact or the cold-elongated configuration. A pictorial description of deformed configurations along with orientation angles is given in Fig. 1. The deformation parameters are also made temperature dependent [33,34], by using the relation

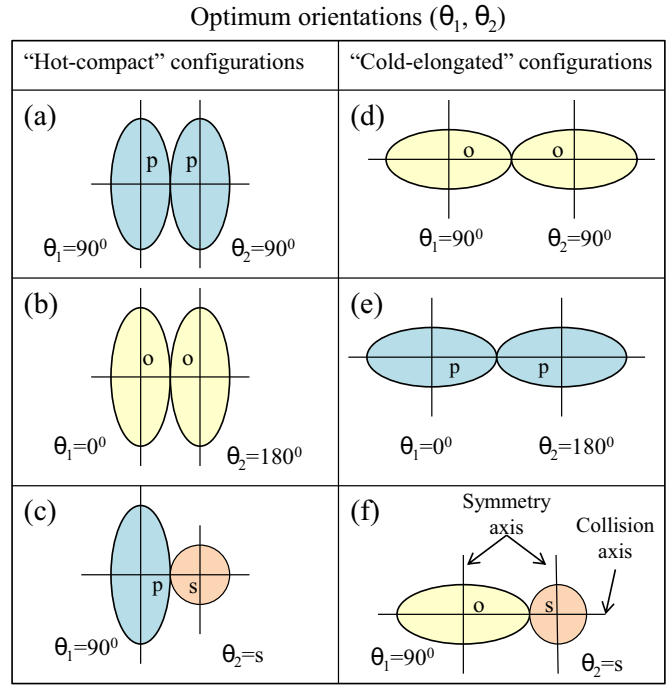

FIG. 1. A pictorial representation of hot-compact (a)–(c) and cold-elongated (d)–(f) configurations for prolate (p), oblate (o), and spherical (s) shapes of nuclei. See Ref. [11] for further details.

$$\beta_{\lambda i}(T) = \exp(-T/T_0)\beta_{\lambda i}(0), \quad (2)$$

where $\beta_{\lambda i}(0)$ represents the static deformation and T_0 is the temperature of the nucleus at which shell effects start to vanish ($T_0 = 1.5$ MeV) [28].

Using the fragmentation potential $V_R(\eta, T)$, the preformation yields $P_0(A_i)$ of the decaying fragments (A_i) is obtained by solving the Schrödinger equation in the η coordinate at fixed $R = R_a$,

$$\left\{-\frac{\hbar^2}{2\sqrt{B_{\eta\eta}}}\frac{\partial}{\partial\eta}\frac{1}{\sqrt{B_{\eta\eta}}}\frac{\partial}{\partial\eta} + V_R(\eta, T)\right\}\psi^\nu(\eta) = E^\nu\psi^\nu(\eta), \quad (3)$$

with $\nu = 0, 1, 2, 3, \ldots$ referring to ground-state ($\nu = 0$) and excited-state solutions, with the ground-state preformation probability P_0 given as

$$P_0 = |\psi(\eta(A_i))|^2\sqrt{B_{\eta\eta}}\frac{2}{A_{\rm CN}}. \quad (4)$$

The higher values of ν contribute to excited states, and these contributions enter via excitation of higher vibrational states. For these excited states, the wave function reads as

$$|\psi|^2 = \sum_{\nu=0}^{\infty}|\psi^\nu|^2\exp(-E^\nu/T). \quad (5)$$

The preformation probability (P_0) is the probability to find certain mass fragments at position R on the decay path and

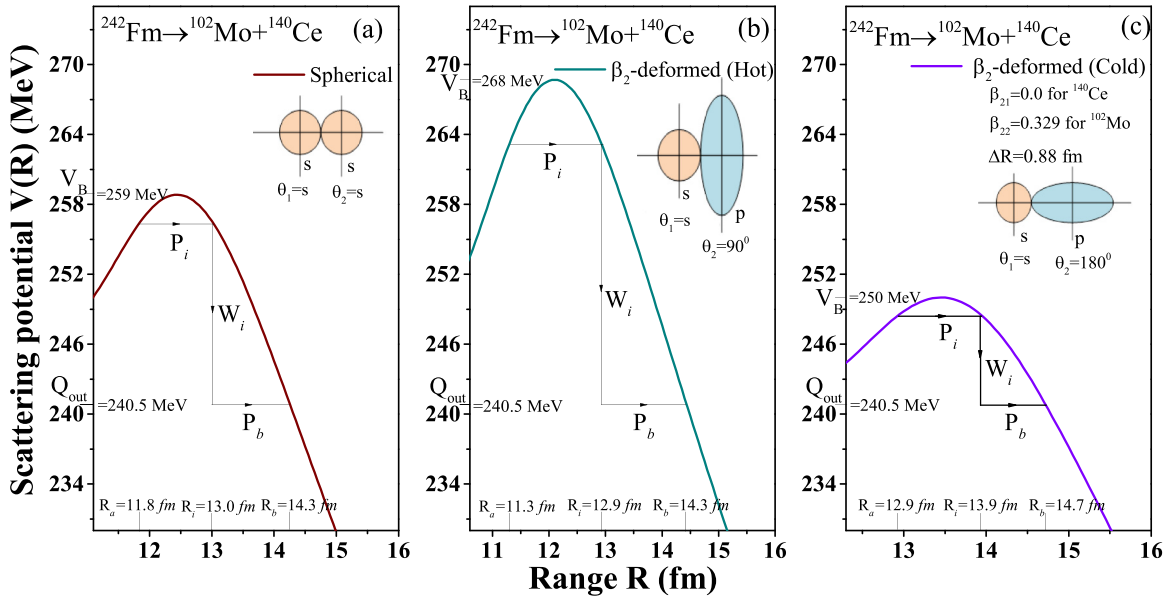

FIG. 2. PCM-calculated scattering *or* interaction potential for (a) spherical, (b) β_2-deformed hot-compact, and (c) β_2-deformed cold-elongated configurations for asymmetric spontaneous fission of the ^{242}Fm nucleus.

is calculated using collective clusterization to estimate the fission products. $B_{\eta\eta}$ in Eq. (4) represents the smooth hydrodynamical mass parameter [35]. The next step is to estimate the penetrability P. For ground-state and excited-state decays, the barrier penetration proceeds differently, which is explained via the PCM and DCM descriptions in the subsequent section.

A. Preformed cluster model

The decay half-life $T_{1/2}$ and the decay constant λ are calculated as

$$T_{1/2} = \frac{\ln 2}{\lambda} = \nu P_0 P. \tag{6}$$

Here, P_0 and P are the preformation probability and the barrier penetrability, referring to η and R motions, respectively. ν_0 is the barrier assault frequency, calculated as

$$\nu_0 = \frac{\text{velocity}}{R_0} = \frac{(2E_2/\mu)^{1/2}}{R_0}, \tag{7}$$

where R_0 is the radius of the parent nucleus, μ is the reduced mass, and E_2 is the kinetic energy related to the Q value, given as $E_2 = (A_1/A)Q$. It is to be noted that the PCM is the $\ell = 0$ and $T = 0$ version of the DCM for ground-state decay processes. To compute the fragmentation potential for ground-state decay analysis, Eq. (1) is solved at $T = 0$ and $\ell = 0$, where P_0 is calculated using Eq. (4) for the $\nu = 0$ vibrational state. In the PCM, the penetration probability P is a three-step process obtained from the Wenzel-Kramers-Brillouin (WKB) integral and is calculated using

$$P = P_a W_i P_b. \tag{8}$$

The transmission probability consists of three contributions as shown in Fig. 2:

(i) the penetrability P_a from R_a to R_i,

$$P_a = \exp\left(-\frac{2}{\hbar}\int_{R_a}^{R_i}\{2\mu[V(R) - V(R_i)]\}^{1/2}dR\right); \tag{9}$$

(ii) the inner deexcitation probability W_i at R_i (and is taken to be unity [36]),

$$W_i = \exp(-bE_i); \tag{10}$$

(iii) the penetrability P_b from R_i to R_b

$$P_b = \exp\left(-\frac{2}{\hbar}\int_{R_i}^{R_b}\{2\mu[V(R) - Q]\}^{1/2}dR\right). \tag{11}$$

In the above equations, $V(R)$ is the scattering potential and is calculated using the relation

$$V(R) = V_P + V_C + V_\ell, \tag{12}$$

where $V_\ell = 0$ for ground-state decays.

B. Dynamical cluster-decay model

For ℓ partial waves, the CN decay or the fragment's production cross section is given by

$$\sigma(A_1, A_2) = \frac{\pi}{k^2}\sum_{\ell=0}^{\ell_{\max}}(2\ell+1)P_0 P, \quad k = \sqrt{\frac{2\mu E_{\text{c.m.}}}{\hbar^2}}, \tag{13}$$

where the preformation probability P_0 is defined by Eqs. (4) and (5) for the excited states ($\nu \neq 0$), and the penetrability P is calculated as shown in Eq. (14), which further depends on the temperature (T) and the angular momentum (ℓ). $\mu = mA_1A_2/(A_1 + A_2)$ is the reduced mass, and $\ell_{\max}$ is maximum angular momentum fixed where the cross sections of light particles (or evaporation residue) become negligibly small.

For investigating the dynamics of an excited compound nucleus, the T-dependent fragmentation potential is calculated using Eq. (1).

In the DCM, the penetrability P is a one-step process (different from the PCM method) and is calculated using the following WKB integral,

$$P = \exp\left(-\frac{2}{\hbar}\int_{R_a}^{R_b}\{2\mu[V(R) - Q_{\rm eff}]\}^{1/2}dR\right), \tag{14}$$

with $V(R_a, T) = V(R_b, T) = \mathrm{TKE}(T) = Q_{\rm eff}(T)$. $V(R_a, T)$ acts like an effective Q value of decay, $Q_{\rm eff}(T)$, and $\mathrm{TKE}(T)$ as the total kinetic energy of decaying fragments. The point (R_a) of the penetration path is defined as

$$\begin{aligned} R_a(T) &= R_1(\alpha_1, T) + R_2(\alpha_2, T) + \Delta R(T) \\ &= R_t(\alpha, T) + \Delta R(T), \end{aligned} \tag{15}$$

with radius vectors R_i ($i = 1$ and 2),

$$R_i(\alpha_i, T) = R_{0i}(T)\left[1 + \sum_\lambda \beta_{\lambda i} Y_\lambda^{(0)}(\alpha_i)\right], \tag{16}$$

and T-dependent nuclear radii $R_{0i}(T)$ of the nuclear system,

$$R_{0i}(T) = R_{0i}(1 + 0.0007T^2)\ \mathrm{fm}. \tag{17}$$

Here, R_{0i} is taken from Refs. [30,31] for the prox00 version of the proximity potential. α_i is the angle between the symmetry axis and the radius vector of the colliding nucleus, and ΔR is the only parameter of the model known as the neck-length parameter, which assimilates the neck formation effects and related deformation effects.

III. CALCULATIONS AND RESULTS

This part is divided into two subsections, i.e., Secs. III A and III B. In the first section, the SF investigation of radioactive Fm isotopes is made; however, the second section is devoted to the ^{11}B-induced fission of Fm nuclei.

A. Spontaneous fission of Fm isotopes

In the PCM, the angular and temperature effects are silent; however, the deformation effects are included up to quadrupole (β_2) deformations of fragments with optimum orientations of decay fragments. Depending on the prolate and oblate shapes (+ and − signs) of β_2 deformations, the orientation angles are uniquely fixed, which results in the "hot-compact" and "cold-elongated" configurations as shown in Fig. 1 (for a detailed description of optimum orientations, see Ref. [11]). The hot-compact and cold-elongated configurations are also known as equatorial (side-side) and polar (tip-tip) configurations, respectively. In this manuscript, we denote hot-compact and cold-elongated configurations as β_2-deformed (hot) and β_2-deformed (cold) orientations. First, the barrier characteristics are analyzed for the asymmetric spontaneous fission of the ^{242}Fm $\rightarrow$ ^{140}Ce ($\beta_{21} = 0.0$) + ^{102}Me ($\beta_{22} = 0.329$) nucleus in reference to these configurations. Figures 2(a), 2(b), and 2(c) show the scattering potential $V(R)$, respectively, for the choice of spherical, β_2-deformed (hot), and β_2-deformed (cold) approaches. It is observed from

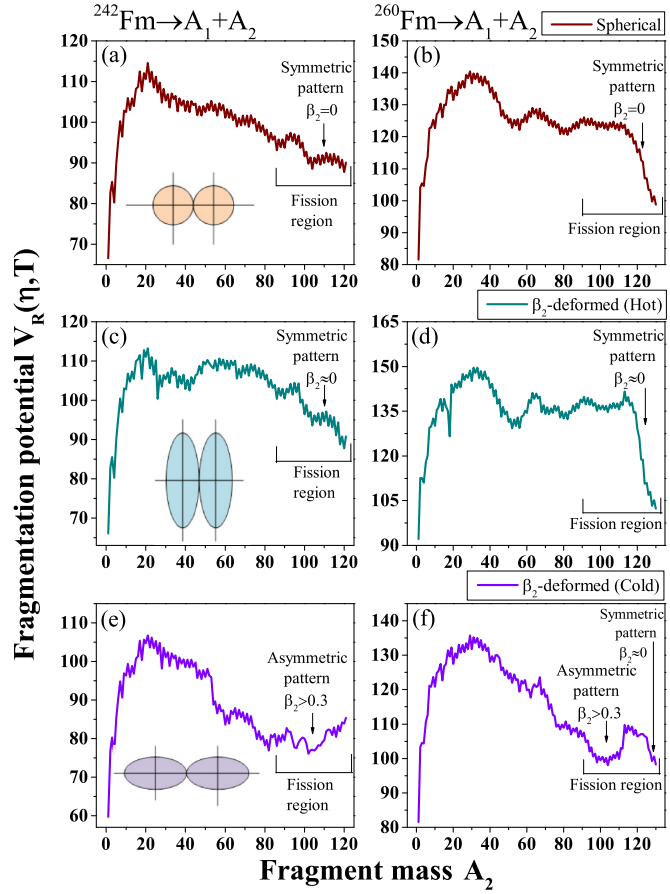

FIG. 3. Collective fragmentation potential $V_R(\eta)$ of ^{242}Fm and ^{260}Fm nuclei for (a), (b) spherical, (c), (d) β_2-deformed (hot), and (e), (f) β_2-deformed (cold) configurations. The fission regions and related β_2 deformations are also marked.

Figs. 1 and 2 that the barrier properties are significantly modified with the inclusion of deformations and orientation effects. The interaction radius is largest for the case of cold configurations and smallest for the hot configuration as evident from Figs. 1 and 2. Consequently, cold orientations correspond to the smallest interaction barrier and hot configurations to the largest interaction barrier. This means that such effects are highly important as they in turn modify the preformation probability P_0, the barrier penetrability P, and hence the decay half-life.

For further analysis of fission valleys, the collective fragmentation potential $V_R(\eta)$ of ^{242}Fm and ^{260}Fm fissioning nuclei is plotted in Figs. 3(a)–3(f) as a function of the light fragment mass (A_2) for the choice of spherical, β_2-deformed (hot), and β_2-deformed (cold) approaches. The structure of fission valleys is significantly modified with the inclusion of deformation and orientation effects. The corresponding fission region is marked in the figure. If we focus on the spherical approach ($\beta_2 = 0$ for each fragmentation), the fission dips indicate that the symmetric fragments are main contributors in the spontaneous fission of ^{242}Fm and ^{260}Fm parent nuclei [see Figs. 3(a) and 3(b)]. The contributed fission fragments of both nuclei in Figs. 3(c) and 3(d) also show the symmetric fission

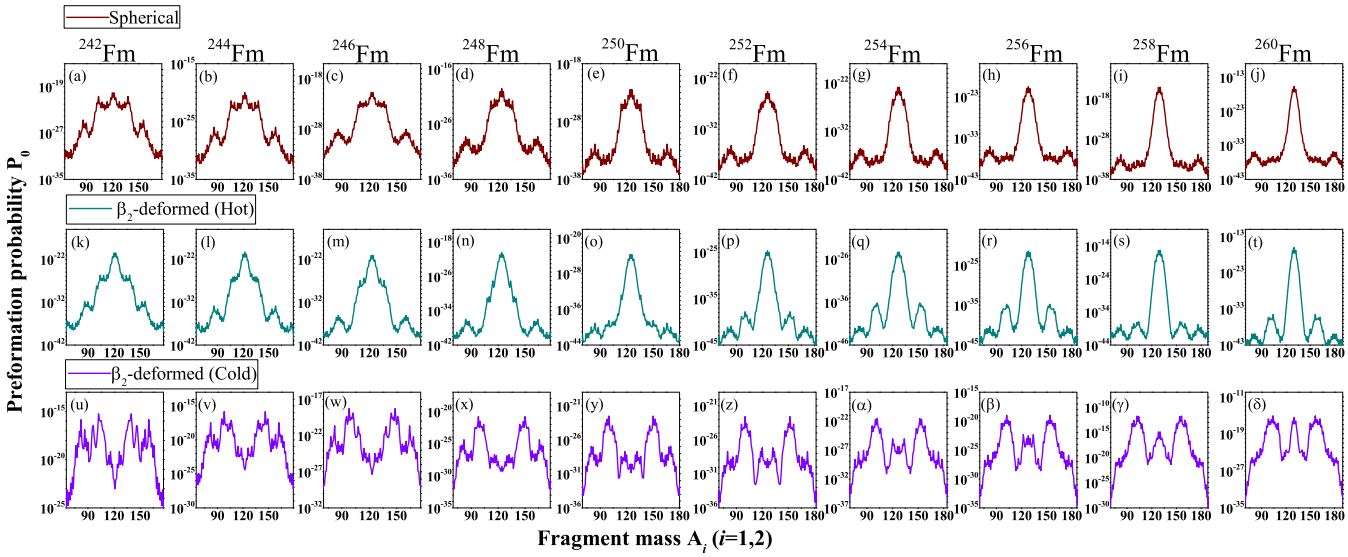

FIG. 4. The preformation yield P_0 is plotted as a function of fission fragments of all considered Fm isotopes for (a)–(j) spherical fragments, (k)–(t) β_2-deformed hot-compact configurations, and (u)–(δ) β_2-deformed cold-elongated configurations.

pattern for the β_2-deformed hot configuration. However, the cold interactions in Figs. 3(e) and 3(f) show a dominance of asymmetric fission and multimodal fission, respectively, for ^{242}Fm and ^{260}Fm nuclei. Here, multimodal fission means the coexistence of both symmetric and asymmetric fission.

It is clear from above analysis that the inclusion of hot or cold orientations cause significant influence on the fragment mass distribution, as the fragmentation potential depends on the deformation parameter and on the choice of radius vector as shown in Eq. (1). For β_2-deformed (hot) cases, the symmetric fission valleys in the fragmentation potential are observed in the neighborhood of spherical or nearly spherical fragments ($\beta_2 \approx 0$). However, for cold configurations, the asymmetric minima in the fragmentation potential correspond to highly deformed fragments ($\beta_2 > 0.3$) where the symmetric one belongs to spherical or nearly spherical nuclei ($\beta_2 \approx 0$).

In hot orientations, the spherical decaying fragments have interaction radii larger than those of the β_2-deformed fragments, and hence the fragmentation potential has a smaller magnitude for spherical fragments; therefore, we get the symmetric distribution for this case. On the other side, the cold-elongated interactions of highly deformed fragments result in the larger interaction radii leading to the lower fragmentation potential as compared to spherical fragments. As a consequence, the asymmetric fission becomes prominent for the case of cold interactions. It will be of further interest to explore the causes and consequences of spherical emergence (symmetric) and deformed (asymmetric) fragments in the cold interaction criteria, for the case of the ^{260}Fm nucleus. For further analysis, the preformation probability P_0 of each isotope of Fm is shown in Figs. 4(a)–4(j), 4(k)–4(t), and 4(u)–4(δ) for spherical, β_2-deformed (hot), and β_2-deformed (cold) approaches, respectively. It is to be noted here that the fragmentation potential goes as an input in the Schrödinger equation used to calculate the preformation probability P_0, and the valleys of the fragmentation potential correspond to the peaks of the preformation probability and vice versa. Overall, the mass distribution of $^{242-260}$Fm isotopes show the symmetric pattern in the fission region for spherical and β_2-deformed (hot) cases. However, the symmetric peak becomes sharper with an increase in the neutron (N) number of the Fm parent nucleus and with the inclusion of β_2-deformed hot orientations in the decay fragments. For the β_2-deformed (cold) case, a transition from double peak to triple peak is observed as one goes from ^{242}Fm to ^{260}Fm fissioning nuclei. This indicates that the β_2-deformed (cold) approach follows a different fission decay path than that of the spherical and hot interactions. The results of the preformation probability shown in Fig. 4 are in agreement with the ones plotted for the fragmentation potential in Fig. 3. The lighter-mass Fm isotopes exhibit asymmetric spontaneous fission. However the mass distributions of the heavier fermium isotope (^{260}Fm) seem to suggest the possibility of multimodal spontaneous fission (that means the coexistence of symmetric and asymmetric fission). This indicates that the cold-elongated configuration results are in reasonable agreement with the experimental observations of Refs. [6–9].

To analyze the multimodal fission of Fm isotopes, the positions of nascent fission fragments in proton (Z) and neutron (N) numbers and the most probable fission fragments are identified in reference to the peaks of the preformation probability P_0. The most probable light (A_L) and heavy (A_H) fission fragments are listed in Table I, and the Z and N numbers of the light fission fragments (A_L) are plotted in Figs. 5(a) and 5(b) as a function of the mass number of the parent nuclei for the spherical and β_2-deformed (cold) approaches. The choice of fission fragments for the β_2-deformed (hot) case is the same as that of the spherical approach. The symmetric peaks for both spherical and hot interactions are mainly governed by the spherical magic shell closures of the proton number at $Z = 50$, which means the $^{242-260}$Fm isotopes decay via isotopes of tin (Sn). The neutron number of these isotopes increases with the mass number of the parent nuclei and approaches the spherical neutron shell closure of $N = 82$ for the

TABLE I. The PCM-calculated SF half-lives $T_{1/2}^{SF}$ are presented along with the fitted neck-length parameter ΔR and the most probable fission fragments for spherical and β_2-deformed (cold) orientations. The calculated half-lives are also compared with the experimental one [37].

Parent nucleus	Decay channel	ΔR (fm)	$\log_{10} T_{1/2}^{SF}$ (sec) PCM	Expt.
		Spherical		
^{242}Fm	^{120}Sn + ^{122}Sn	1.418	−1.586	−3.097
^{244}Fm	^{122}Sn + ^{122}Sn	1.420	−1.600	−2.481
^{246}Fm	^{122}Sn + ^{124}Sn	1.369	−0.826	0.903
^{248}Fm	^{124}Sn + ^{124}Sn	1.372	5.247	4.556
^{250}Fm	^{124}Sn + ^{126}Sn	1.000	7.353	7.402
^{252}Fm	^{126}Sn + ^{126}Sn	0.640	9.606	9.596
^{254}Fm	^{126}Sn + ^{128}Sn	0.640	7.291	7.294
^{256}Fm	^{128}Sn + ^{128}Sn	0.653	4.023	4.019
^{258}Fm	^{128}Sn + ^{130}Sn	1.100	−3.440	−3.432
^{260}Fm	^{130}Sn + ^{130}Sn	0.725	−2.372	−2.397
		β_2-deformed		
^{242}Fm	^{102}Mo + ^{140}Ce	0.880	−2.928	−3.097
^{244}Fm	^{98}Zr + ^{146}Nd	0.760	−2.268	−2.481
^{246}Fm	^{98}Zr + ^{148}Nd	0.480	0.860	0.903
^{248}Fm	^{98}Zr + ^{150}Nd	0.180	4.767	4.556
^{250}Fm	^{100}Zr + ^{150}Nd	0.015	7.397	7.402
^{252}Fm	^{100}Zr + ^{152}Nd	0.001	7.615	9.596
^{254}Fm	^{102}Zr + ^{152}Nd	0.083	6.228	7.294
^{256}Fm	^{102}Zr + ^{154}Nd	0.274	2.455	4.019
^{258}Fm	^{102}Zr + ^{156}Nd	0.660	−3.339	−3.432
	^{128}Sn + ^{130}Sn	1.050	−3.439	
^{260}Fm	^{104}Zr + ^{156}Nd	0.582	−2.324	−2.397
	^{130}Sn + ^{130}Sn	0.670	−2.382	

heaviest considered isotope. For the β_2-deformed (cold) case, the Z number and the N number of light asymmetric fission fragments lie in the neighborhood of the deformed magic shell closures of $Z = 38$ and $N = 60$ and 62. This indicates that deformed magic shell closures play an important role in the case of cold-elongated configurations. However, the symmetric peak becomes more prominent in heavier-mass $^{258-260}$Fm nuclei and belongs to the spherical doubly magic shell closures of the Sn ($Z = 50$, $N = 82$) nuclei. From Figs. 3–5, it may be concluded that the spherical and deformed magic shell closures along with the deformation and orientation degree of freedom play an important role in the division of a fissioning nucleus. The SF half-lives ($T_{1/2}^{SF}$) of identified fission fragments are calculated by using the only parameter of the PCM, i.e., the "neck-length" parameter (ΔR) for spherical and β_2-deformed (cold) cases. Table I and Fig. 6(c) represent the PCM-calculated half-lives, which show nice agreement with the experimental data [37]. For the case of ^{258,260}Fm nuclei, the half-lives are calculated for both symmetric fission and asymmetric fission fragments as both nuclei show multimodal fission in cold interactions. The fission half-lives and the neck-length parameters along with the identified most probable fission fragments are listed in Table I. The magnitude of ΔR is small for cold interactions in comparison to the spherical approach. The decay half-life depends on the

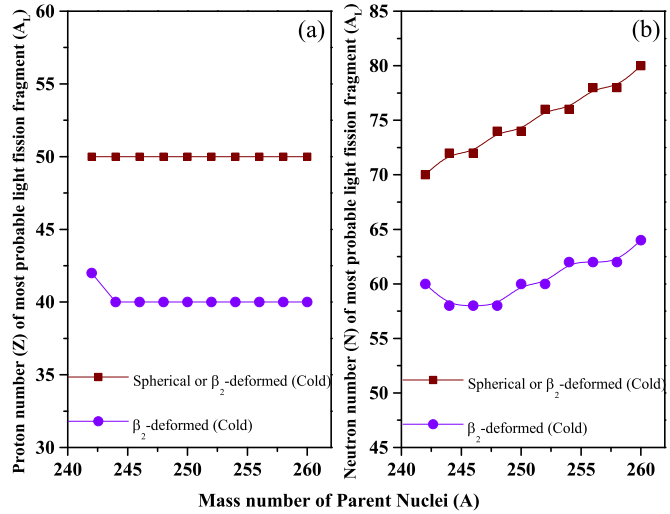

FIG. 5. (a) Proton (Z) and (b) neutron (N) numbers of most preferred light fission fragments are plotted as a function of mass of Fm spontaneous fissioning nuclei for spherical and β_2-deformed (cold) cases.

preformation probability P_0 and the penetrability P as per Eq. (6). Figures 6(a), 6(b), and 6(c) depict $\log_{10} P_0$, $\log_{10} P$, and $\log_{10} T_{1/2}^{SF}$ of the most favorable fission fragments, respectively, as a function of the mass number of the parent nuclei. It is clear from figure that $\log_{10} T_{1/2}^{SF}$ show the opposite trend to $\log_{10} P_0$ and $\log_{10} P$. It is clearly evident from Fig. 6 that, when preformation and penetration probabilities are large, the decay half-life is small and vice versa. This indicates that the higher probability of fragment preformation and the subsequent penetration lead to lower magnitude of the decay half-life. This justifies the fact that the preformation factor and the barrier penetrability are highly desirable for adequate addressal of the SF mechanism.

B. Induced fission of Fm isotopes

In the previous section we have explored the spontaneous fission of Fm isotopes and investigated the fission mass distribution for the spherical as well as the deformed choice of decay fragments in the collective clusterization process. Further, to analyze the excitation energy (E_{CN}^*) and angular momentum (ℓ) effects on fission fragment mass distributions, the excited-state fission decay analysis of Fm isotopes formed in the heavy-ion-induced reactions is carried out in this section. Previously, one of us and collaborators have made an investigation of the ^{254}Fm* nucleus formed in the ^{11}B + ^{243}Am reaction at various excitation energies using the spherical approach, the β_2 deformation, and higher multipole (β_2–β_4) deformations within the DCM [12]. This work explored some interesting results with regard to the effects of deformations, orientations, and excitation energies. As an expansion of this work, we have chosen ^{11}B-induced reactions on $^{231-249}$Am targets forming hot and rotating $^{242-260}$Fm* isotopes to analyze the fission fragment mass distributions.

First, the fragmentation potential $V_R(\eta, T)$ and the preformation probability P_0 of the ^{242}Fm* nucleus formed via

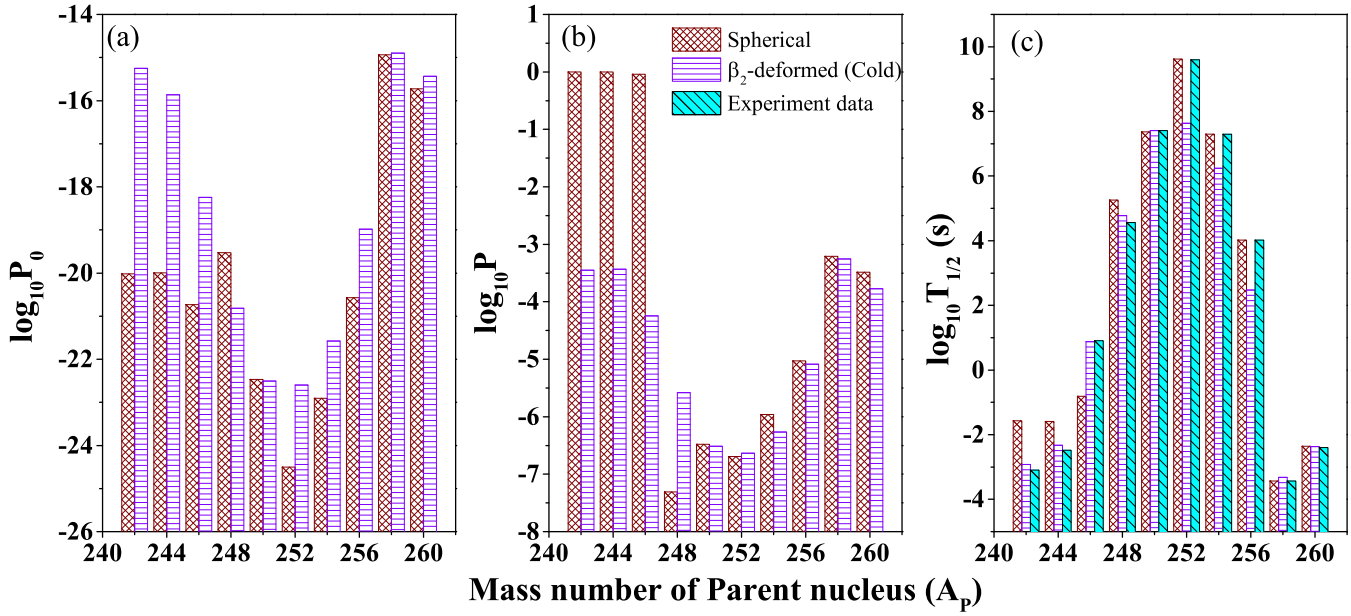

FIG. 6. The logarithm of (a) the preformation probability ($\log_{10} P_0$), (b) the penetrability ($\log_{10} P$), and (c) the SF half-lives ($\log_{10} T^{\rm SF}_{1/2}$ (s)) as a function of the mass number of Fm isotopes for spherical, β_2-deformed (hot), and β_2-deformed (cold) configurations.

the $^{11}\mathrm{B} + ^{231}\mathrm{Am}$ reaction at excitation energy $E^* = 42$ MeV are calculated for three kinds of approaches as used for the case of spontaneous fission, such as spherical, β_2-deformed (hot), and β_2-deformed (cold) configurations of decay fragments [see Figs. 7(a) and 7(b)]. In Figs. 7(a) and 7(b), the deformations are considered T-independent, i.e., static deformations [$\beta_2(0)$]. The calculations are made at $\Delta R =$ 1.0 fm in reference to work on $^{254}\mathrm{Fm}^*$ at the same excitation energy [12]. It is evident from Fig. 7 that the structure of the fragmentation potential is significantly modified with the inclusion of deformations and orientations. The mass distribution shows asymmetric behavior for β_2-deformed (cold) configurations. However, the broad symmetric pattern of the spherical approach changes to a sharp symmetric fission peak for the hot configuration. The reason behind these structural variations of the fragmentation potential and the preformation probability is similar to one explored for spontaneous fission, discussed in Sec. III A. The results for hot-compact configurations are in agreement with those of a previous study [12]. It was observed that various Fm isotopes show symmetric fission fragment mass distributions for static and dynamic β_2-deformed hot-compact orientations [12]. In Fig. 7, the cold-elongated configuration represents the asymmetric fission mass distribution in agreement with the experimental observation of Refs. [9,38,39]. Therefore, further analysis is carried out for the choice of β_2-deformed cold-elongated configurations only.

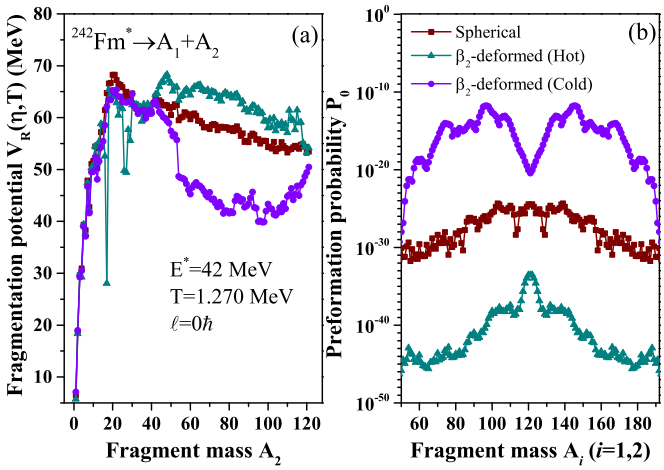

FIG. 7. (a) Fragmentation potential $V_R(\eta)$ and (b) preformation probability P_0 of the $^{242}\mathrm{Fm}^*$ nucleus plotted as a function of fragment mass for spherical, β_2-deformed (hot), and β_2-deformed (cold) configurations.

To explore the temperature (T) dependence on deformation for cold-elongated orientations, a comparative analysis of T-independent (static) and T-dependent (dynamic) β_2 deformations is made in Figs. 8(a) and 8(b) and Figs. 8(c) and 8(d), respectively, for $^{242}\mathrm{Fm}^*$ and $^{260}\mathrm{Fm}^*$ excited nuclei at $E^* = 42$ MeV and $\ell = 0\hbar$. It is seen from Fig. 8 that the dynamic deformations [$\beta_{2i}(T)$] impart significant influence on the fragmentation path and the preformation distribution. The static deformations [$\beta_{2i}(0)$] follow an asymmetric fission pattern for both fissioning nuclei. In the case of dynamic deformations, the $^{242}\mathrm{Fm}^*$ nucleus exhibits broad mass distribution (mix of symmetric and asymmetric components), whereas a clear symmetric peak appears in the mass distribution of the $^{260}\mathrm{Fm}^*$ nucleus. This indicates that dynamic deformations have great influence on the fission fragment mass distributions and show nice agreement with the experimental observations [9,38].

The above results are plotted at zero angular momentum (i.e., $V_\ell = 0$) only, the ℓ dependence on fragment mass distribution is explored via Eq. (1). Figures 9(a) and 9(b) show the preformation probability for $^{242}\mathrm{Fm}^*$ and $^{260}\mathrm{Fm}^*$ nuclei for cold interactions using dynamic deformations in a broad range

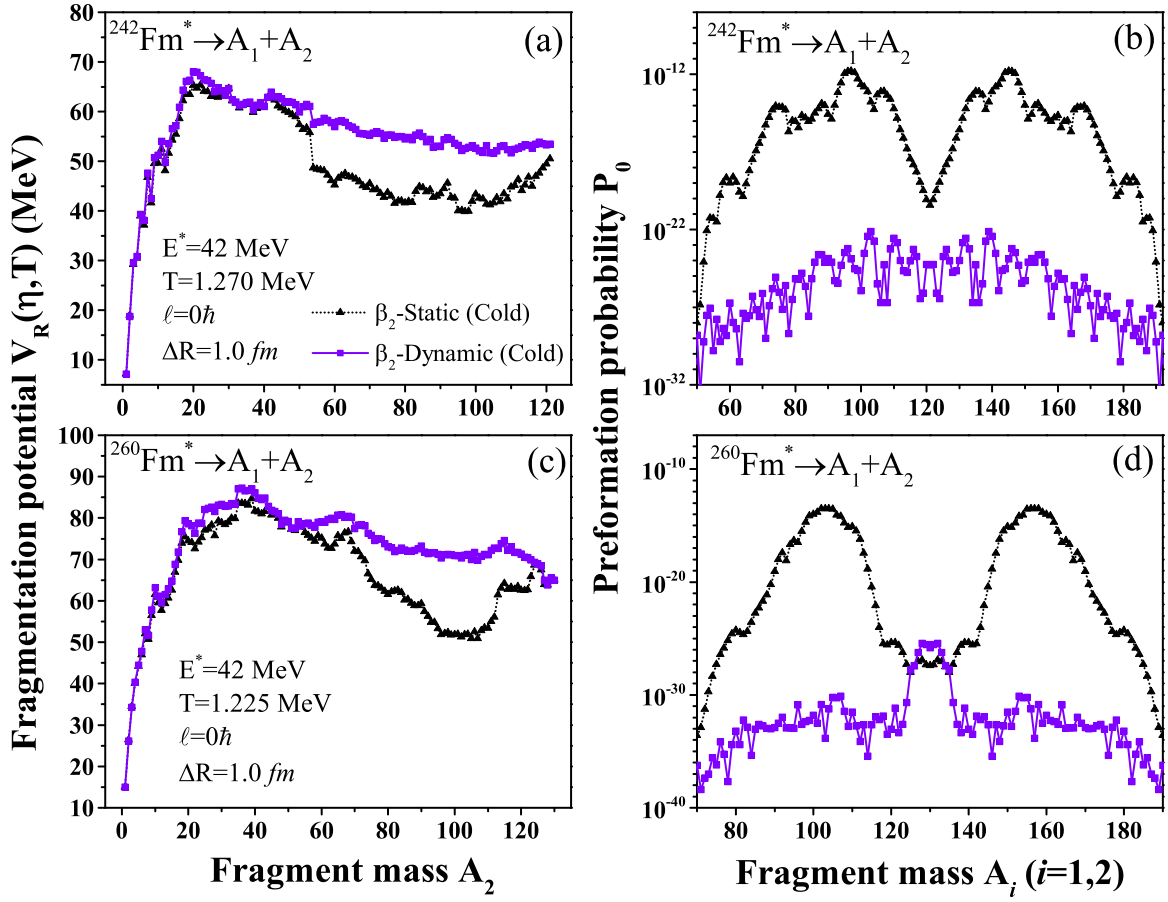

FIG. 8. DCM-calculated (a), (c) fragmentation potential $V(A_2)$ and (b), (d) preformation probability P_0 for ^{242}Fm* and ^{260}Fm* nuclei are plotted for static (T-independent) and dynamic (T-dependent) deformations for cold orientations.

of angular momenta, i.e., $\ell = 0$-$\ell_{\max}$ at $E^* = 42$ MeV. There are some structural variations in the structure of P_0 for both nuclei. However, the overall mass distribution of fission fragments remains similar, i.e., broad spectrum (near asymmetric) for ^{242}Fm* and symmetric distribution for ^{260}Fm* nucleus.

ΔR is the only parameter of the model that is used to address the experimental half-lives and decay cross sections. However, in the present case our main focus is to analyze mass distributions of Fm isotopes. To analyze the impact of ΔR

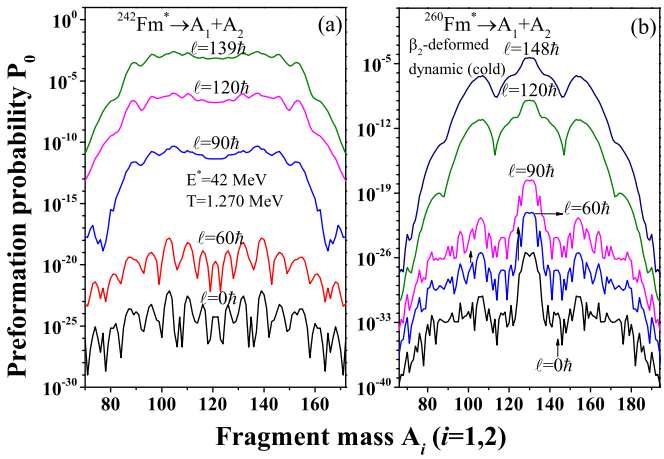

FIG. 9. Preformation probability (P_0) as a function of fragment mass (A_i) for (a) ^{242}Fm* and (b) ^{260}Fm* nuclei at angular momentum values $\ell = 0$–$\ell_{\max}$.

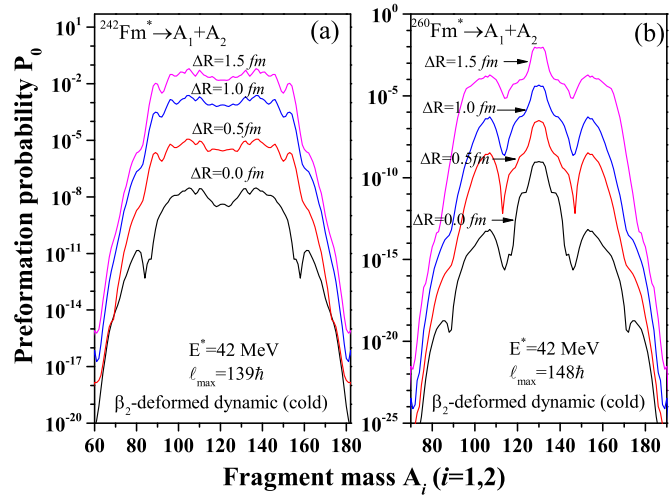

FIG. 10. The preformation probability $P_0(A_i)$ is presented for a neck-length parameter range of $\Delta R = 0$–1.5 fm for (a) ^{242}Fm and (b) ^{260}Fm compound nuclei.

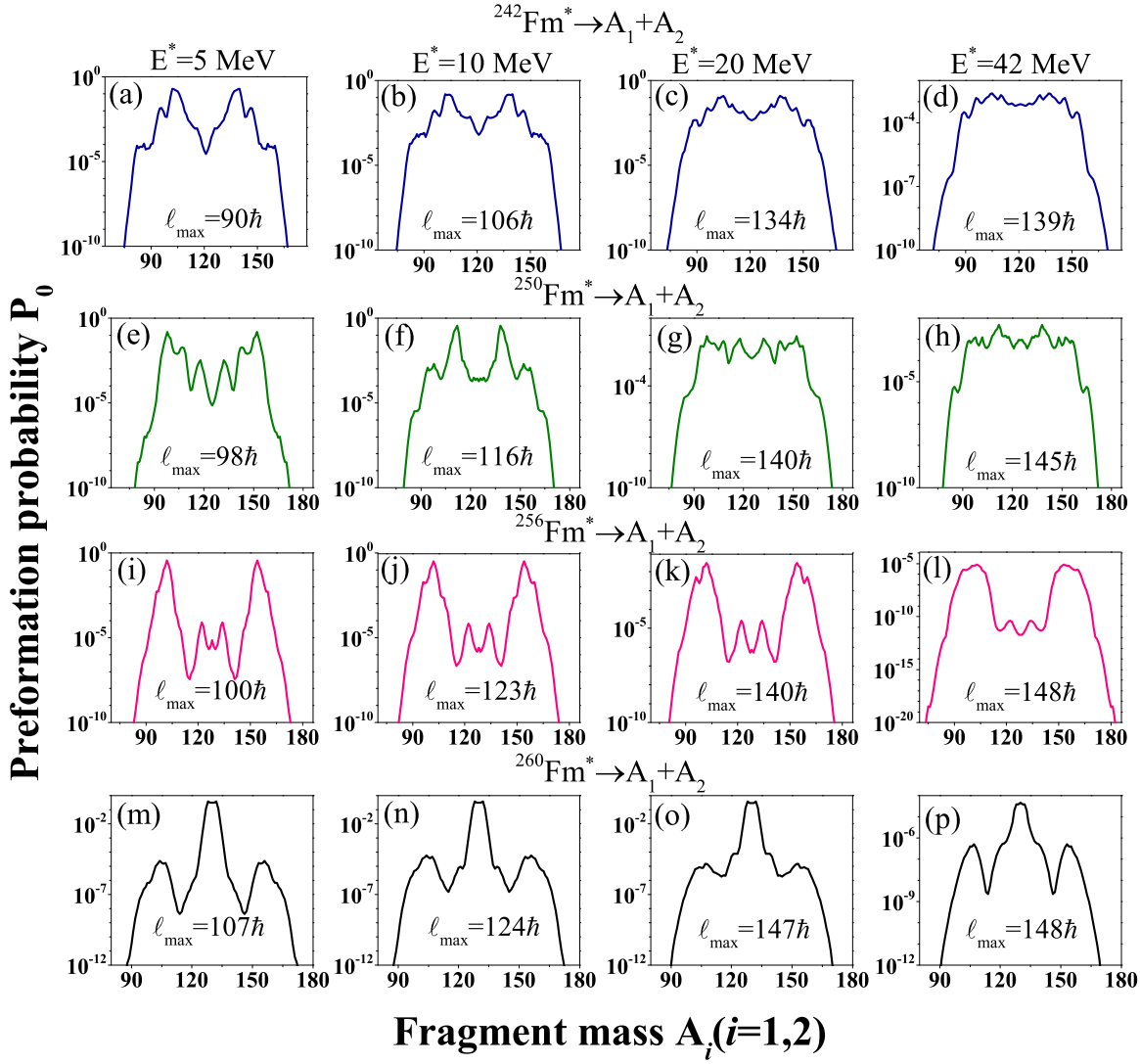

FIG. 11. The preformation yield $P_0(\mathrm{A}_i)$ of ^{242,250,256,260}Fm fissioning nuclei is plotted at excitation energies $E^* = 5$, 10, 20, and 42 MeV.

on the mass distributions, the preformation yield P_0 is plotted in Figs. 10(a) and 10(b), respectively, for ^{242}Fm* and ^{260}Fm* nuclei at $E^* = 42$ MeV for $\Delta R = 0.0$ to 1.5 fm. It is clearly evident that the magnitude of P_0 increases with increments in ΔR. However, the fission pattern remains similar, i.e., near asymmetric for ^{242}Fm* and symmetric for ^{260}Fm*. That means ΔR does not clearly affect the fission decay channel of the considered fissioning nuclei.

Finally, the energy dependence of fission fragment mass distributions of ^{242,250,256,260}Fm* isotopes is studied in Fig. 11 at excitation energies $E^* = 5$, 10, 20, and 42 MeV and corresponding ℓ_{max} values for the cold-elongated orientation case. It is clearly observed from Fig. 11 that fission fragment mass distributions are significantly modified with increase in excitation energy and neutron numbers of compound nuclei. The evolution towards mass asymmetry slows down with increases in excitation energies for ^{242,250,256}Fm* [see Figs. 11(a)–11(l)]. This can be easily understood from the fact that shell effects start diminishing with increases in energy [28]. However, the ^{260}Fm* nucleus prefers to decay via symmetric fragments at all energies. If we compare spontaneous fission versus induced fission from Figs. 4 and 5 for cold interactions, it is observed that for both cases lighter-mass Fm nuclei prefer asymmetric fission distribution. For heavier-mass Fm nuclei, the triple-humped distribution is observed for the case of spontaneous fission showing the significant contribution of asymmetric components along with dominant symmetric fragments. However, at various excitation energies the symmetric fission is the more dominant decay mode in comparison with asymmetric fission, as one can see from Figs. 11(m)–11(p). These results are in fair agreement with the induced fission measurements of Refs. [9,38,39].

IV. SUMMARY

First, the spontaneous fission of $^{242-260}$Fm isotopes is studied within the preformed cluster model. We have computed the fission fragment mass distributions for three types of decay configurations: spherical, quadrupole β_2-deformed hot-compact, and β_2-deformed cold-elongated. The interaction

radius decreases as one goes from cold-elongated to spherical to hot-compact shapes, whereas the interaction barrier height increases as one goes from cold-elongated to spherical to hot-compact configurations of decay fragments. These results affect the barrier characteristics and hence the fragmentation path, because the potentials involved strongly depend on the deformation and the interaction radius of decay fragments. The spherical and β_2-deformed hot-compact configurations depict the symmetric pattern for each fermium isotope; however, the symmetric peaks become sharp with increases in the neutron (N) number of the parent nucleus. The β_2-deformed cold-elongated shapes of decay fragments show a transition from double-humped (asymmetric fission) to triple-humped (multimodal fission) mass distribution. The heavier isotopes such as $^{258-260}$Fm exhibit multimodal fission (i.e., coexistence of both symmetric and asymmetric fission) for the cold configuration criteria. Spherical and β_2-deformed hot-compact approaches show that Fm isotopes decay via spherical magic shell closure [Sn ($Z = 50$) isotopes]. However, for cold orientations, Fm nuclei prefer to decay via asymmetric fragments having deformed magic shell closures of $Z = 38$ and $N = 60$ and 62. From this, we conclude that spherical as well as deformed magic shell closures play an important role in the fission dynamics of Fm isotopes. The decay half-lives of the considered spontaneous fissioning nuclei are calculated and have nice agreement with the experimental data.

Next, the induced fission of $^{242-260}$Fm* compound nuclei formed via ^{11}B + $^{231-249}$Am reactions at excitation energies $E^* = 5$–42 MeV is investigated using the dynamical cluster-decay model for the choice of cold-elongated configurations of fragments. We have observed that the T-dependent (dynamic) deformations play a significant role in fission fragment mass distributions. A transformation from an asymmetric to a symmetric fission peak is observed with an increase in the neutron number of the Fm* nucleus. Moreover, the excitation energies of fissioning nuclei significantly affect the fission mass distributions. The angular momentum (ℓ) and the neck-length parameter (ΔR) dependence of mass distributions are studied and it is observed that magnitude of preformation yields significant changes; however, the overall fission decay pattern remains the same.

The present study highlights the significance of deformation and orientation effects, together with the excitation energy and the isotope dependence of fission fragment mass distributions for both spontaneous and induced fission dynamics. It will be of further interest to investigate the ternary fission (i.e., the division of fissioning nuclei into three fragments) of Fm isotopes in reference to the structure of the fragmentation potential and fission yields.

ACKNOWLEDGMENT

The financial support from the UGC-DAE Consortium for Scientific Research, File No. UGC-DAE-CSR-KC/CRS/19/NP09/0920, is gratefully acknowledged.

[1] N. Bohr and J. A. Wheeler, Phys. Rev. **56**, 426 (1939).
[2] U. Brosa, S. Grossmann, and A. Müller, Phys. Rep. **197**, 167 (1990).
[3] A. N. Andreyev *et al.*, Phys. Rev. Lett. **105**, 252502 (2010).
[4] A. N. Andreyev, M. Huyse, and P. Van Duppen, Rev. Mod. Phys. **85**, 1541 (2013).
[5] I. V. Ryzhov *et al.*, Phys. Rev. C **83**, 054603 (2011).
[6] J. P. Balagna, G. P. Foxd, D. C. Hoffman, and S. D. Knight, Phys. Rev. Lett. **26**, 145 (1971).
[7] J. E. Gindler, K. F. Flynn, L. E. Glendenin, and R. K. Sjoblom, Phys. Rev. C **16**, 1483 (1977).
[8] E. K. Hulet *et al.*, Phys. Rev. C **40**, 770 (1989).
[9] K. F. Flynn, J. E. Gindler, and L. E. Glendenin, Phys. Rev. C **12**, 1478 (1975).
[10] K. Nishio, H. Ikezoe, S. Mitsuoka, I. Nishinaka, Y. Nagame, Y. Watanabe, T. Ohtsuki, K. Hirose, and S. Hofmann, Phys. Rev. C **77**, 064607 (2008).
[11] R. K. Gupta, M. Balasubramaniam, R. Kumar, N. Singh, M. Manhas, and W. Greiner, J. Phys. G: Nucl. Part. Phys. **31**, 631 (2005).
[12] M. Kaur, M. K. Sharma, and R. K. Gupta, Phys. Rev. C **86**, 064610 (2012).
[13] N. Sharma, A. Kaur, and M. K. Sharma, Phys. Rev. C **102**, 064603 (2020).
[14] K. Sharma, G. Sawhney, and M. K. Sharma, Phys. Rev. C **96**, 054307 (2017).
[15] G. Sawhney, M. K. Sharma, and R. K. Gupta, Phys. Rev. C **83**, 064610 (2011).
[16] K. Sharma, G. Sawhney, M. K. Sharma, and R. K. Gupta, Nucl. Phys. A **972**, 1 (2018).
[17] A. Kaur and M. K. Sharma, Phys. Rev. C **99**, 044611 (2019).
[18] A. Kaur and M. K. Sharma, Eur. Phys. J. A **55**, 89 (2019).
[19] G. Kaur, K. Sandhu, A. Kaur, and M. K. Sharma, Phys. Rev. C **97**, 054602 (2018).
[20] A. Kaur, G. Kaur, S. K. Patra, and M. K. Sharma, Nucl. Phys. A **990**, 94 (2019).
[21] B. B. Singh, M. K. Sharma, and R. K. Gupta, Phys. Rev. C **77**, 054613 (2008).
[22] H. J. Fink, J. Maruhn, W. Scheid, and W. Greiner, Z. Phys. **268**, 321 (1974).
[23] J. Maruhn and W. Greiner, Phys. Rev. Lett. **32**, 548 (1974).
[24] R. K. Gupta, W. Scheid, and W. Greiner, Phys. Rev. Lett. **35**, 353 (1975).
[25] N. J. Davidson, S. S. Hsiao, J. Markram, H. G. Miller, and Y. Tzeng, Nucl. Phys. A **570**, 61 (1994).
[26] P. A. Seeger, Nucl. Phys. **25**, 1 (1961).
[27] W. Myers and W. J. Swiatecki, Nucl. Phys. **81**, 1 (1966).
[28] A. S. Jensen and J. Damgaard, Nucl. Phys. A **203**, 578 (1973).
[29] V. M. Strutinsky, Nucl. Phys. A **95**, 420 (1967).
[30] R. Kumar and M. K. Sharma, Phys. Rev. C **85**, 054612 (2012).
[31] W. D. Myers and W. J. Swiatecki, Phys. Rev. C **62**, 044610 (2000).

[32] P. Möller, J. R. Nix, W. D. Myers, and W. J. Swiatecki, At. Data Nucl. Data Tables **59**, 185 (1995).
[33] M. Muenchow and W. Scheid, Phys. Lett. B **162**, 265 (1985); Nucl. Phys. A **468**, 59 (1987).
[34] M. Rashdan, A. Faessler, and W. Waida, J. Phys. G: Nucl. Part. Phys. **17**, 1401 (1991).
[35] H. Kröger and W. Scheid, J. Phys. G: Nucl. Part. Phys. **6**, L85 (1980).
[36] M. Greiner and W. Scheid, J. Phys. G: Nucl. Part. Phys. **12**, L229 (1986).
[37] N. E. Holden and D. C. Hoffman, Pure Appl. Chem. **72**, 1525 (2000).
[38] K. F. Flynn, J. E. Gindler, R. K. Sjoblom, and L. E. Glendenin, Phys. Rev. C **11**, 1676 (1975).
[39] R. C. Ragaini, E. K. Hulet, R. W. Lougheed, and J. Wild, Phys. Rev. C **9**, 399 (1974).